A Hybrid Wavelet Expansion and Boundary Element Analysis for Multiconductor Transmission Lines in Multilayered Dielectric Media

Gaofeng Wang, Guangwen Pan, *Senior Member, IEEE,* and Barry K. Gilbert, *Senior Member, IEEE*

Abstract— **In this paper the wavelet expansion method, in conjunction with the boundary element method (BEM), is applied for the evaluation of the capacitance and inductance matrices of multiconductor transmission lines in multilayered dielectric media. The integral equations obtained by using a Green's function above a ground plane are solved by Galerkin's method, with the unknown total charge expanded in terms of orthogonal wavelets in $L^2([0, 1])$. The difficulty of using wavelets on the real line to expand unknown functions defined in finite intervals is overcome by the utilization of wavelets in $L^2([0, 1])$. The adoption of the geometric representation of the BEM converts the two-dimensional problem into a one-dimensional problem, and provides a versatile and accurate treatment of curved conductor surfaces and dielectric interfaces. A sparse matrix equation is developed from the set of integral equations, which is extremely valuable, in particular when a large system of equations must be solved. Finally, we compare our numerical results with previously published data, and demonstrate good agreement between the two sets of results.**

I. Introduction

WAVELET analysis has drawn a great deal of attention in both applied mathematics and many engineering disciplines in recent years. Wavelet techniques have been found to have two major applications in engineering. As a transform, the wavelet transform outperforms Fourier analysis since the wavelet transform preserves information from the signal in the original spatial domain, which the Fourier transform (series) does not provide. Moreover, in contrast to the conventional short-duration Fourier transform that has fixed resolutions in both time and frequency, the wavelet transform provides a multiresolution analysis in which multilevel resolutions in both the time and frequency domains can be attained. The wavelet transform has become a popular and useful tool in image analysis and signal processing [1]–[3]. When employed as a basis set, the cancellation property of the wavelet allows the generation of sparse matrices, which speeds up the solution of integral equations. Recently, applications of wavelets as bases or wavelet-like basis functions are becoming widely used in the solution of electromagnetic modeling problems [4]–[7].

Manuscript received October 12, 1993; revised June 8, 1994. This work was supported in part by ARPA/ESTO under Contract N00014-91-J-4030 from the Office of Naval Research and by Boeing Aerospace Co. under Contract 133-P771.

G. Wang is with the Tanner Research, Inc., Pasadena, CA 91107 USA.

G. Pan is with the Department of Electrical Engineering, University of Wisconsin–Milwaukee, Milwaukee, WI 53201 USA.

B. K. Gilbert is with the Mayo Foundation, Rochester, MN 55905 USA.

IEEE Log Number 9407465.

Among the various wavelet forms, orthogonal wavelets appear to be the most useful in numerical analysis [7]. In [8], orthogonal wavelets on the real line were applied to expand integral operators and demonstrated remarkable operator compressions; however, only Calderon–Zygmund type kernels were investigated. Unfortunately, the integral equations arising in electromagnetic problems essentially are not members of this class. Moreover, the work in [8] did not address the difficulty of using wavelets on the entire real line to expand the unknown function on a finite portion of the real line. In [6] wavelets were applied to a real world electromagnetic modeling problem, in which electromagnetic fields coupled through a double-slot aperture in a planar conducting screen separating two identical half-space regions. In this approach the integral kernel (the second Hankel function $H_0^{(2)}(2\pi|x - x'|)$ of order zero) and the unknown equivalent magnetic current were expanded in terms of the Battle–Lemarie wavelet in $\boldsymbol{L}^2(\boldsymbol{R})$. Since this wavelet has infinite support, the wavelet was truncated at the boundary points. Hence, a nonphysical solution at the boundary points was produced. As a result, some undesired oscillations near the boundaries can be observed in the numerical example presented in Fig. 4 of [6] for the magnitude of the equivalent magnetic current obtained from the truncated Battle–Lemarie wavelet.

A full wave analysis of microstrip floating line structures was obtained by using a wavelet expansion method in [7], where a Sommerfeld-type integral with a much more intractable kernel (the dyadic Green's functions for the grounded dielectric slab) was treated by using Daubechies' wavelet, one type of orthogonal wavelet with compact support on the real line. Since the Daubechies' wavelet has compact support, one can easily delete the wavelet bases or scaling functions that are beyond the regions of interest, and thus the truncation of the wavelet at the boundary points is avoided. As mentioned in [7], an edge basis is required at each end of the finite intervals to guarantee the completeness of the basis. The problems treated in [6]–[8] were essentially in straight line domains. Since most practical problems exhibit complicated geometries, it is more desirable to be able to handle curves and surfaces.

Multiple-conductor, multiple-transmission line systems are commonly found in high-speed, high-density digital electronics, at the levels of individual chip carriers, printed circuit boards, and more recently, multichip modules (MCM's). Although previous methods for extraction of the distributed

circuit parameters including more rigorous theories [9]–[11] and even full-wave analysis techniques [12], [13], the quasi-TEM solutions are still widely used in digital design [14]–[18], since the bandwidths of the digital signals are still below approximately 10 GHz and the dimensions of the conductors on typical printed circuit boards are fairly large in comparison to the skin depth in the metals, although shrinking rapidly [19].

In this paper, we present a new approach for extraction of the capacitance and inductance matrices of multiconductor transmission lines in multilayered dielectric media by using the wavelet expansion method in combination with the BEM. Almost all the integral paths in this problem are closed or can properly be mapped into closed grouped contours, as long as the unknown charge distribution is continuous along the entire grouped contour, and has the same value at its two end points. Therefore, it is possible to employ periodic orthogonal wavelets in $L^2([0, 1])$ as basis functions to expand the unknown charge distributions, provided that one can form proper maps between the integral paths (including both the closed contours and the grouped contours) and the simplex interval [0, 1].

The utilization of the wavelet in $L^2([0, 1])$ has two advantages: No truncation of the wavelet is needed at the boundaries, and the wavelet offers a complete basis in the regions of interest. In order to treat the curved conductor surfaces or dielectric interfaces, the geometric representation in the BEM is incorporated into this analysis. The paper is organized as follows. In Section II the periodic orthogonal wavelet theory is reviewed briefly, followed by a brief summary of the integral equation formulation in Section III. Section IV is dedicated to the implementation of the wavelet expansion method and the geometric description using the conventional BEM. Numerical examples are presented in Section V.

II. Orthogonal Wavelets in $L^2([0, 1])$

In this section, several results of wavelet theory relevant to this work will be reviewed briefly. More comprehensive discussions of wavelets can be found in monographs and books (e.g., [20]–[22]).

A natural way to describe wavelets is multiresolution analysis (MRA). A nested sequence of closed subspaces $\boldsymbol{V}_m$ is said to generate a multiresolution analysis in $\boldsymbol{L}^2(\boldsymbol{R})$ if it satisfies the following properties:

$$\cdots \subset \boldsymbol{V}_{-1} \subset \boldsymbol{V}_0 \subset \boldsymbol{V}_1 \subset \boldsymbol{V}_2 \subset \cdots \tag{1}$$

$$clos_{\boldsymbol{L}^2}\left(\bigcup_{m\in\boldsymbol{Z}} \boldsymbol{V}_m\right) = \boldsymbol{L}^2(\boldsymbol{R}),\ \bigcap_{m\in\boldsymbol{Z}} \boldsymbol{V}_m = \{\emptyset\} \tag{2}$$

$$f(x) \in \boldsymbol{V}_m \Leftrightarrow f(2x) \in \boldsymbol{V}_{m+1} \tag{3}$$

$$f(x) \in \boldsymbol{V}_0 \Leftrightarrow f(x-n) \in \boldsymbol{V}_0 \tag{4}$$

where $m, n \in \boldsymbol{Z}$ and $\boldsymbol{Z}$ denotes the set of integers. Properties (1) and (2) imply that the projection of a function in a subspace $\boldsymbol{V}_m$ contains more information than its projection in the lower subspace $\boldsymbol{V}_{m-1}$, and ensure that every function in $\boldsymbol{L}^2(\boldsymbol{R})$ can be approximated as closely as desired by its projection in $\boldsymbol{V}_m$, which converges to the original function as m approaches ∞. Properties (3) and (4) tell us that the subspaces can be derived from one another through dilation by a factor of two, and are invariant under integer translations.

It can be shown that for each such nested subspace sequence $\{\boldsymbol{V}_m\}_{m\in\boldsymbol{Z}}$, there exists a unique function $\phi(x) \in \boldsymbol{L}^2(\boldsymbol{R})$, called the scaling function, such that its dilating and translating versions

$$\phi_{m.n}(x) = 2^{m/2}\phi(2^m x - n) \tag{5}$$

form an orthonormal basis of the closed subspace $\boldsymbol{V}_m$ for m, $n \in \boldsymbol{Z}$. For any function $f(x) \in \boldsymbol{L}^2(\boldsymbol{R})$, an approximation can be obtained by its projection in $\boldsymbol{V}_m$

$$f(x) \simeq \boldsymbol{A}_m f(x) \equiv \sum_n \overline{f}_{m,n}\phi_{m,n}(x) \tag{6}$$

where $\boldsymbol{A}_m$ is the orthogonal projection operator onto $\boldsymbol{V}_m$, and $\overline{f}_{m,n}$ is the inner product of $f(x)$ and $\phi_{m,n}(x)$. The projection $\boldsymbol{A}_m f(x)$ is often called an approximation of the function $f(x)$ at the resolution 2^m. The difference of the information between $\boldsymbol{A}_m f(x)$ and $\boldsymbol{A}_{m-1}f(x)$ is contained in the orthogonal complement $\boldsymbol{W}_{m-1}$ of $\boldsymbol{V}_{m-1}$ in $\boldsymbol{V}_m$. The subspaces $\{\boldsymbol{W}_m\}_{m\in\boldsymbol{Z}}$ are called wavelet subspaces. Moreover, it can be shown that there exists a function $\psi(x) \in \boldsymbol{L}^2(\boldsymbol{R})$, called the "mother wavelet," such that its dilating and translating versions

$$\psi_{m,n}(x) = 2^{m/2}\psi(2^m x - n) \tag{7}$$

form an orthonormal basis of $\boldsymbol{W}_m$. Since $\boldsymbol{V}_{m+1} = \boldsymbol{V}_m \oplus \boldsymbol{W}_m$ for any $m \in \boldsymbol{Z}$, from (2) it follows that

$$\bigoplus_{m\in\boldsymbol{Z}} \boldsymbol{W}_m = \boldsymbol{L}^2(\boldsymbol{R}) \tag{8}$$

and thus $\{\psi_{m,n}\}_{m,n\in\boldsymbol{Z}}$ is an orthonormal basis of $\boldsymbol{L}^2(\boldsymbol{R})$. By using this fact, (6) can be written as

$$f(x) \simeq \boldsymbol{A}_m f(x) = \boldsymbol{A}_{m_1} f(x) + \sum_{m'=m_1}^{m-1} \boldsymbol{B}_{m'} f(x) \tag{9}$$

with

$$\boldsymbol{B}_{m'} f(x) \equiv \sum_n \tilde{f}_{m'n}, \psi_{m'n}(x)$$

where $m_1 \leq m-1$ and $\tilde{f}_{m',n}$ is the inner product of $f(x)$ and $\psi_{m',n}(x)$. If m_1 goes to $-\infty$, the first term becomes zero in (9) and a "pure" wavelet expansion is rendered.

Given a multiresolution analysis with scaling function $\phi(x)$ and wavelet $\psi(x)$ in $\boldsymbol{L}^2(\boldsymbol{R})$, we can construct the wavelet in $\boldsymbol{L}^2([0, 1])$ [20] by defining

$$\phi^{per}_{m,n}(x) = \sum_{k\in\boldsymbol{Z}} \phi_{m,n}(x+k) \tag{10}$$

$$\psi^{per}_{m,n}(x) = \sum_{k\in\boldsymbol{Z}} \psi_{m,n}(x+k) \tag{11}$$

and $\boldsymbol{V}^{per}_m = clos_{\boldsymbol{L}^2([0,1])}\{\phi^{per}_{m,n}(x) : n \in \boldsymbol{Z}\}$, $\boldsymbol{W}^{per}_m = clos_{\boldsymbol{L}^2([0,1])}\{\psi^{per}_{m,n}(x) : n \in \boldsymbol{Z}\}$. It can be shown that $\boldsymbol{V}^{per}_m$ are all identical one-dimensional spaces containing only the

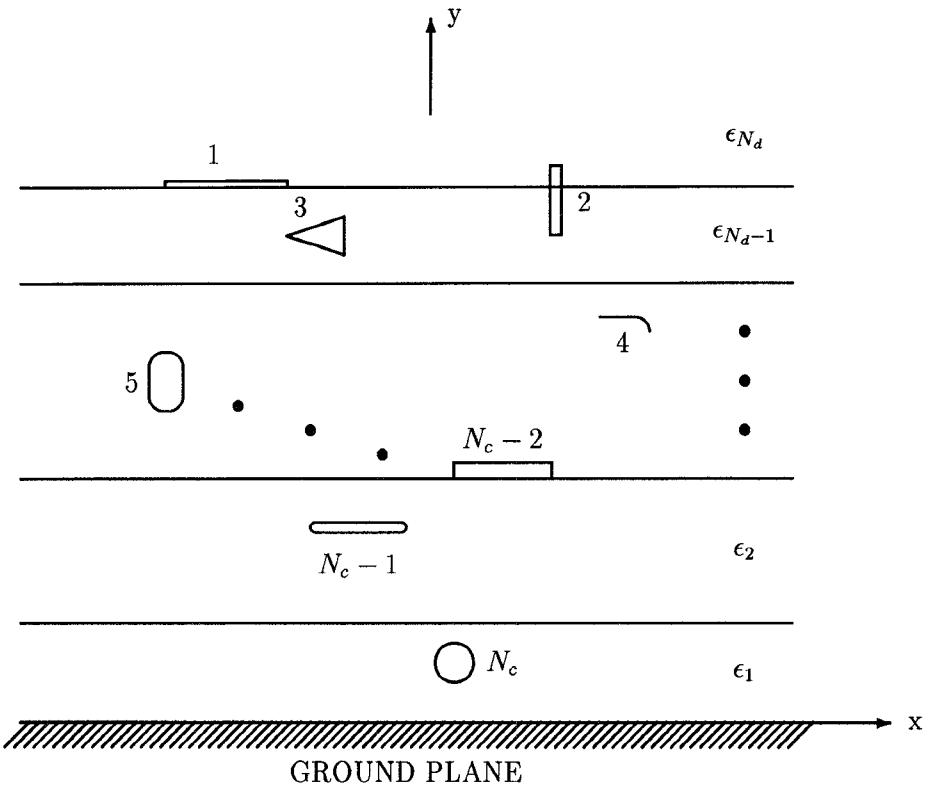

Fig. 1. Configuration of multiconductor transmission line systems in multilayered dielectric media.

constant functions for $m \leq 0$, and $\boldsymbol{W}_m^{per} = \{\emptyset\}$ for $m \leq -1$. Thus we only need to study $\boldsymbol{V}_m^{per}$ and $\boldsymbol{W}_m^{per}$ for $m \geq 0$. Moreover, it can easily be verified that

$$\boldsymbol{V}_{m+1}^{per} = \boldsymbol{V}_m^{per} \oplus \boldsymbol{W}_m^{per} \tag{12}$$

and

$$clos_{\boldsymbol{L}^2}\left(\bigcup_{m\in\boldsymbol{N}} \boldsymbol{V}_m^{per}\right) = \boldsymbol{L}^2([0,1]) \tag{13}$$

where $\boldsymbol{N}$ is the set of nonnegative integers. Hence, there is a ladder of multiresolution spaces,

$$\boldsymbol{V}_0^{per} \subset \boldsymbol{V}_1^{per} \subset \boldsymbol{V}_2^{per} \subset \cdots \tag{14}$$

with successive orthogonal complements $\boldsymbol{W}_0^{per}$, $\boldsymbol{W}_1^{per}$, $\boldsymbol{W}_2^{per}$, $\cdots$, and orthonormal bases $\{\phi_{m,n}^{per}(x)\}_{n=0,\cdots,2^m-1}$ in $\boldsymbol{V}_m^{per}$, $\{\psi_{m,n}^{per}(x)\}_{n=0,\cdots,2^m-1}$ in $\boldsymbol{W}_m^{per}$ for $m \in \boldsymbol{N}$. In particular. $\{\phi_{0,0}^{per}\} \cup \{\psi_{m,n}^{per} : m \in \boldsymbol{N}, n = 0, \cdots, 2^m - 1\}$ constitute an orthonormal basis in $\boldsymbol{L}^2([0, 1])$. For simplicity, this basis is relabeled as follows:

$$\begin{aligned}
g_0(x) &= \phi_{0,0}^{per}(x) = 1 \\
g_1(x) &= \psi_{0,0}^{per}(x) \\
g_2(x) &= \psi_{1,0}^{per}(x) \\
g_3(x) &= \psi_{1,1}^{per}(x) = g_2(x - \tfrac{1}{2}) \\
&\vdots \\
g_{2^m}(x) &= \psi_{m,0}^{per}(x) \\
&\vdots \\
g_{2^m+n}(x) &= \psi_{m,n}^{per}(x) \\
&= g_{2^m}(x - n2^{-m}) 0 \leq n \leq 2^m - 1. \\
&\vdots
\end{aligned} \tag{15}$$

For any $f(x) \in \boldsymbol{L}^2([0, 1])$, its approximation at the resolution 2^m can be defined as the projection in $\boldsymbol{V}_m^{per}$:

$$f(x) \simeq \boldsymbol{P}_m f(x) = \sum_{k=0}^{2^m-1} f_k g_k(x) \tag{16}$$

where $\boldsymbol{P}_m$ is the orthogonal projection operator onto $\boldsymbol{V}_m^{per}$ and f_k is the inner product of $f(x)$ and $g_k(x)$.

III. Integral Equations and Functional Formulation

Fig. 1 shows the transmission line system under consideration. An arbitrary number of conductors N_c is embedded in a dielectric slab, consisting of an arbitrary number of individual layers N_d. A perfectly conducting ground plane extends from $x = -\infty$ to $x = \infty$. The system is uniform in the z direction. The conductors are perfectly lossless and can be of either a finite cross section or infinitesimally thin.

For the above system, the integral equation formulation was derived in detail in [15]. For ease of reference, we briefly quote the major equations here. The integral equations solved for the unknown total charge distribution $\sigma_T(\vec{\rho})$ can be obtained

as follows:

$$\frac{1}{2\pi\epsilon_0}\sum_{j=1}^{J}\int_{l_j}\sigma_T(\vec{\rho}')\ln\frac{|\vec{\rho}-\vec{\rho}''|}{|\vec{\rho}-\vec{\rho}'|}\,dl' = V_c(\vec{\rho}) = \text{constant} \tag{17}$$

on the conductor-to-dielectric interface, and

$$\frac{\epsilon^+(\vec{\rho})+\epsilon^-(\vec{\rho})}{2\epsilon_0[\epsilon^+(\vec{\rho})-\epsilon^-(\vec{\rho})]}\sigma_T(\vec{\rho}) + \frac{1}{2\pi\epsilon_0}\sum_{j=1}^{J}\oint_{l_j}\sigma_T(\vec{\rho}')\cdot\left(\frac{\vec{\rho}-\vec{\rho}'}{|\vec{\rho}-\vec{\rho}'|^2}-\frac{\vec{\rho}-\vec{\rho}''}{|\vec{\rho}-\vec{\rho}''|^2}\right)\cdot\hat{n}(\vec{\rho}')\,dl' = 0 \tag{18}$$

on the dielectric-to-dielectric interface, where l_j is the contour of the jth interface above the ground plane, $\vec{\rho}''$ is the image point of $\vec{\rho}'$ about the ground plane, and J is the total number of the interfaces (including conductor-to-dielectric interfaces and dielectric-to-dielectric interfaces); $\oint$ denotes the Cauchy principal value of the integral, and $\hat{n}(\vec{\rho})$ is the unit normal vector at $\vec{\rho}$; The side of the curve l_j is referred to as the "positive" side if $\hat{n}(\vec{\rho})$ points outward the curve, while the other side of the curve is called its "negative" side; $\epsilon^+(\vec{\rho})$ and $\epsilon^-(\vec{\rho})$ denote the permittivity on the positive and negative sides, respectively, of the interface toward which $\vec{\rho}$ approaches.

In order to obtain the capacitance matrix $[C]$, the above integral equations must first be solved for the total charge distribution $\sigma_T(\vec{\rho})$, with V_c assigned to be a unity voltage on each particular conductor surface l_j, and assigned to be a zero voltage on the other conductors. After obtaining the total charge distribution $\sigma_T(\vec{\rho})$, the free charge distribution $\sigma_F(\vec{\rho})$ on the conductors can be evaluated by

$$\sigma_F(\vec{\rho}) = \frac{\epsilon(\vec{\rho})}{\epsilon_0}\sigma_T(\vec{\rho}) \tag{19}$$

for the conductors of finite cross-section, and

$$\sigma_F(\vec{\rho}) = \frac{\epsilon^+(\vec{\rho})+\epsilon^-(\vec{\rho})}{2\epsilon_0}\sigma_T(\vec{\rho}) + \frac{\epsilon^+(\vec{\rho})-\epsilon^-(\vec{\rho})}{2\pi\epsilon_0}\sum_{j=1}^{J}\oint_{l_j}\sigma_T(\vec{\rho}')\cdot\left(\frac{\vec{\rho}-\vec{\rho}'}{|\vec{\rho}-\vec{\rho}'|^2}-\frac{\vec{\rho}-\vec{\rho}''}{|\vec{\rho}-\vec{\rho}''|^2}\right)\cdot\hat{n}(\vec{\rho})\,dl' \tag{20}$$

for the infinitesimally thin strips. The total free charge Q_i (per unit length in the z direction) on conductor l_i corresponding to this potential distribution yields the element C_{ij} ($i, j = 1, 2, \cdots, N_c$) of the capacitance matrix. The inductance matrix $[L]$ is related to the vacuum capacitance matrix $[C_v]$ by the simple formula $[L] = \epsilon_0\mu_0[C_v]^{-1}$. The vacuum capacitance matrix $[C_v]$ itself is the capacitance matrix of the same conductor system with all dielectrics replaced by vacuum.

The previous integral equations (17) and (18) need to be solved numerically for the unknown charge distribution $\sigma_T(\vec{\rho})$. The unknown charge distribution on each interface is expanded in terms of basis functions (described later):

$$\sigma_T(\vec{\rho}) \simeq \sum_{m=1}^{M} g_{m-1}(\vec{\rho})\sigma_{Tm} \tag{21}$$

where $g_{m-1}(\vec{\rho})$ ($m = 1, 2, \cdots, M$) are the basis functions, σ_{Tm} ($m = 1, 2, \cdots, M$) are the unknown coefficients to be determined, and M is the total number of the bases. The reader should not be confused by the fact that, for simplicity of notation, the basis function here is denoted by the same symbol g as the periodized wavelet in the preceding section, since later we will see that there is an inherent relationship between them.

Galerkin's method is used for the testing procedure. Using (21), a set of linear algebraic equations in matrix form can be derived from integral (17) and (18) [18]:

$$[A_{nm}][\sigma_{Tm}] = [B_n] \tag{22}$$

where the elements of the matrices are given as:

$$A_{nm} = \sum_{j1=1}^{J}\int_{l_{j1}} g_{n-1}(\vec{\rho})\cdot\left[\frac{1}{2\pi\epsilon_0}\sum_{j2=1}^{J}\int_{l_{j2}} g_{m-1}(\vec{\rho}')\cdot\ln\left(\frac{|\vec{\rho}-\vec{\rho}''|}{|\vec{\rho}-\vec{\rho}'|}\right)dl'\right]dl \tag{23}$$

$$B_n = \sum_{j1=1}^{J}\int_{l_{j1}} g_{n-1}(\vec{\rho})V_c(\vec{\rho})\,dl \tag{24}$$

for those $g_{n-1}(\vec{\rho})$ defined on the conductor-to-dielectric interfaces, and

$$A_{nm} = \sum_{j1=1}^{J}\int_{l_{j1}} g_{n-1}(\vec{\rho})\cdot\left[\frac{\epsilon^+(\vec{\rho})+\epsilon^-(\vec{\rho})}{2\epsilon_0[\epsilon^+(\vec{\rho})-\epsilon^-(\vec{\rho})]}g_{m-1}(\vec{\rho}) + \frac{1}{2\pi\epsilon_0}\sum_{j2=1}^{J}\oint_{l_j} g_{m-1}(\vec{\rho}')\cdot\left(\frac{\vec{\rho}-\vec{\rho}'}{|\vec{\rho}-\vec{\rho}'|^2}-\frac{\vec{\rho}-\vec{\rho}''}{|\vec{\rho}-\vec{\rho}''|^2}\right)\cdot\hat{n}(\vec{\rho})\,dl'\right]dl \tag{25}$$

$$B_n = 0 \tag{26}$$

for those $g_{n-1}(\vec{\rho})$ defined on the dielectric-to-dielectric interfaces.

After A_{nm} ($n = 1, 2, \cdots, M$; $m = 1, 2, \cdots, M$) and B_n ($n = 1, 2, \cdots, M$) are calculated, (22) produces M simultaneous equations in M unknowns, σ_{Tm} ($m = 1, 2, \cdots, M$). These simultaneous equations can then be solved for σ_{Tm} ($m = 1, 2, \cdots, M$) in terms of the potential $V_c(\vec{\rho})$ on the conductors.

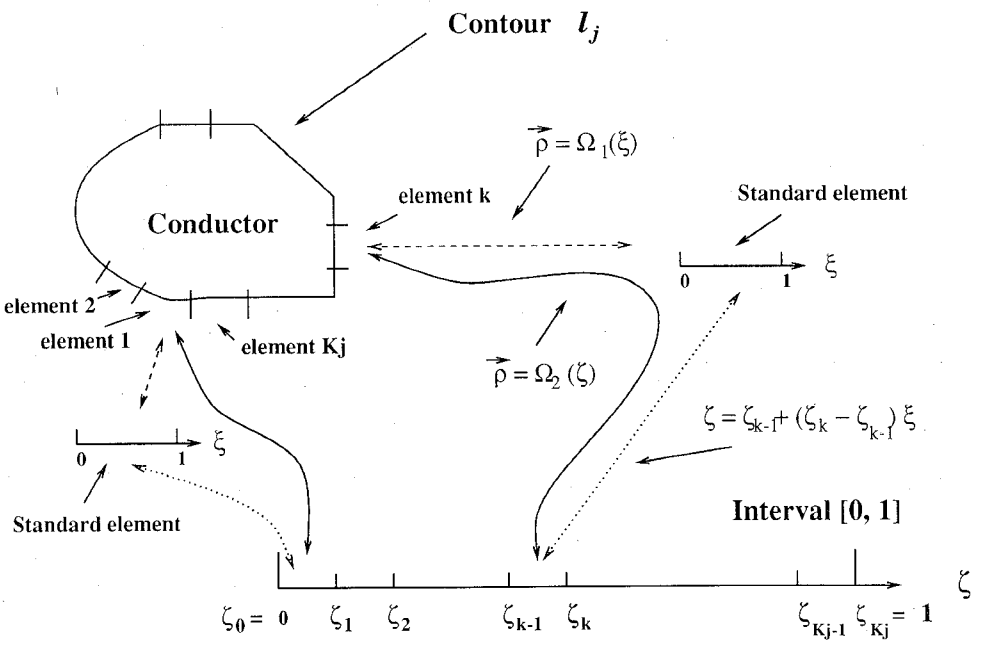

Fig. 2. Mapping between the contour of a conductor with finite cross-section and interval [0, 1].

IV. The Wavelet Expansion and the Boundary Element Method

So far we have not defined the forms of the basis functions, nor have we described how to handle the interfaces, which may be arbitrary surfaces (curves). In other words, the representations of sources and boundary surfaces (curves) have still not been specified. The orthogonal wavelets in $\boldsymbol{L}^2([0, 1])$ and the boundary element method (BEM) [18], [24] are utilized for these purposes.

A. Geometrical Representation

Before considering the details of this problem, we will assume that all contours $\{l_j\}$ are closed for the purpose of expressing the unknown charge distribution. Roughly speaking, there are four types of contours: (a) the contour of the conductor with finite cross section; (b) the contour along the infinitesimally thin metal strip; (c) the contour along the dielectric-to-dielectric interface from $-\infty$ to $+\infty$; and (d) the contour along the dielectric-to-dielectric interface from $-\infty$ to $+\infty$, with some spaces of discontinuity wherever there is a conductor along the interface.

We examine the four types of contours one by one. In the first place, all the contours except type (d) are geometrically continuous. Moreover, the contour of type (a) is closed geometrically. The contour of type (b) can be considered as closed since the charge distribution has the same behavior (singularity) at its two edge points. Similarly, the contour of type (c) can also be viewed as closed, due to the fact that no charge exists at infinity, and thus the charge distribution gives the same value (zero!) at its two ends ($-\infty$ and $+\infty$).

For the contour of type (d), the contour intersects the conductor at a pair of points if the conductor is lying along the contour and creating a discontinuity space for the contour. Generally, the charge distribution gives the same behavior at the two intersection points. If we imagine connecting each of the intervals of this contour, which are separated by the discontinuity space created by the conductors, into a continuous, grouped contour through the pairs of intersection points, the charge distribution can be considered as continuous along the continuous, grouped contour. Therefore, the contour of type d) can also be considered closed as far as the charge distribution is concerned.

Since the periodized wavelets are defined in $\boldsymbol{L}^2([0, 1])$, one would like to map each of the contours $\{l_j\}$ into the interval [0, 1]. For an arbitrary contour l_j, we take two steps:

1) Use the conventional boundary element method to discretize the contour into a series of boundary elements, and then map each of the boundary elements into one-dimensional standard elements through the shape functions or interpolation functions [18], [24];
2) Map the standard elements into corresponding portions of interval [0, 1]. A linear map is good enough for this step.

Fig. 2 gives a diagrammatic illustration of the procedures described above for the contour of a conductor with finite cross-section.

This procedure can be precisely formulated in mathematical language as well. In step 1), the global coordinates $\vec{\rho}$ are expressed in terms of the local coordinate ξ of a standard element [18]:

$$\vec{\rho} = \sum_{i=1}^{M_e} N_i(\xi)\vec{\rho}_i = \Omega_1(\xi) \tag{27}$$

where M_e is the number of the interpolation nodes in the local standard element, $N_i(\xi)$ is the shape function referred to node i of the local standard element, and $\vec{\rho}_i$ are the global coordinates of node i of the actual element. The shape functions $\{N_i(\xi)\}$ are given in standard finite element or boundary element books and literatures (e.g., [18], [24]).

Inspecting (27), it can be concluded that (27) maps the standard element in local coordinates into the actual element, which may have a quite arbitrary or distorted shape, in global coordinates. The node $\vec{\rho}_i$ in the actual element corresponds to the node i in the standard element (by definition, $N_i(\xi)$ is assumed to be a unity value at node i and zero at all other nodes of the element).

In step 2, the standard elements corresponding to the actual elements from contour l_j are mapped into the subintervals $[\zeta_0, \zeta_1]$, $[\zeta_1, \zeta_2]$, $\cdots$, $[\zeta_{K_j-1}, \zeta_{K_j}]$ of interval [0, 1], where K_j is the number of the elements from contour l_j and $0 = \zeta_0 < \zeta_1 < \zeta_2 < \cdots < \zeta_{K_j} = 1$ (for instance, one can simply assume $\zeta_k = k/K_j$, $k = 1, \cdots, K_j - 1$). The map between the local coordinate ζ in interval [0, 1] and the local coordinate ξ in the kth standard element of contour l_j can be written as

$$\zeta = \zeta_{k-1} + (\zeta_k - \zeta_{k-1}) \cdot \xi \tag{28}$$

or

$$\xi = \frac{\zeta - \zeta_{k-1}}{\zeta_k - \zeta_{k-1}} \tag{29}$$

where $k = 1, 2, \cdots, K_j$. Combining (27) and (29), we obtain a map between the global coordinates $\vec{\rho}$ and the local coordinate ζ in interval [0, 1]:

$$\vec{\rho} = \Omega_1\left(\frac{\zeta - \zeta_{k-1}}{\zeta_k - \zeta_{k-1}}\right) = \Omega_2(\zeta). \tag{30}$$

The maps (27)–(30) establish the conversions among the local coordinate ξ, the local coordinate ζ and the global coordinates $\vec{\rho}$.

B. Source Representation

Now we can define the basis functions $\{g_{m-1}(\vec{\rho})\}$. For simplicity and generality, the basis functions will not directly be defined over all the contours in terms of a set of global coordinates, but rather over interval [0, 1], since each of the contours can be related to interval [0, 1] through the map described by (30). By using the conversion between the global coordinates $\vec{\rho}$ and the local coordinate ζ for each individual contour, we can easily obtain the basis functions of the individual contour in the set of global coordinates. For the unknown charge distribution along contour l_j, expansion (21) can now accurately be written as the projection in $\boldsymbol{V}_{m_h}^{per}$ (about ζ):

$$\sigma_T(\vec{\rho}) \simeq \boldsymbol{P}_{m_h}\sigma_T(\vec{\rho}) = \sum_{m=1}^{M_j} g_{m-1}[\Omega_2^{-1}(\vec{\rho})]\sigma_{Tm} \tag{31}$$

where Ω_2^{-1} denotes the inverse map of Ω_2, $g_{m-1}(\zeta)$ represents the orthogonal wavelets in $\boldsymbol{L}^2([0, 1])$, and $M_j = 2^{m_h}$ is the number of the wavelet bases used for expressing the unknown charge distribution on contour l_j. Because Ω_2^{-1} maps contour l_j into interval [0, 1], the basis functions $\{g_{m-1}[\Omega_2^{-1}(\vec{\rho})]\}$ are well-defined.

It can be shown that, if σ_T is smooth function with a finite number of discontinuities, the error between $\sigma_T(\zeta)$ and $\boldsymbol{P}_{m_h}\sigma_T(\zeta)$ is bounded as follows [22]:

$$||\sigma_T(\zeta) - \boldsymbol{P}_{m_h}\sigma_T(\zeta)|| \le C2^{-m_h s} \tag{32}$$

where C and s are some positive constants, respectively, relating to $||\sigma_T(\zeta)||$ and the smoothness of $\sigma_T(\zeta)$. The function $\sigma_T(\zeta)$ with higher order (piecewise) continuity has larger s value and thus faster error decay. Moreover, the approximation error of expansion (31) can be estimated as

$$\begin{aligned} &||\sigma_T(\vec{\rho}) - \boldsymbol{P}_{mh}\sigma_T(\vec{\rho})|| \\ &\quad \le C_d||\sigma_T(\zeta) - \boldsymbol{P}_{m_h}\sigma_T(\zeta)|| \\ &\quad \le CC_d2^{-m_h s} \end{aligned} \tag{33}$$

where C_d is the tight upper bound of the Jacobian of the transformation $\Omega_2(\zeta)$. That is, the approximation error of (31) has exponential decay with respect to the resolution level m_h.

C. Matrix Equation

Based on the above source expansion, a set of linear algebraic equations can be obtained from integral equation (17) and (18) by using Galerkin's method. Its matrix form is described by (22), if the elements of the matrices are computed by replacing $\{g_{m-1}(\vec{\rho})\}$ with $\{g_{m-1}[\Omega_2^{-1}(\vec{\rho})]\}$ in (23)–(26), namely,

$$\begin{aligned} A_{nm} = \sum_{j1=1}^{J}\int_{l_{j1}} & g_{n-1}[\Omega_2^{-1}(\vec{\rho})] \\ & \cdot \left[\frac{1}{2\pi\epsilon_0}\sum_{j2=1}^{J}\int_{l_{j2}} g_{m-1}[\Omega_2^{-1}(\vec{\rho}')] \right. \\ & \left. \cdot \ln\left(\frac{|\vec{\rho} - \vec{\rho}''|}{|\vec{\rho} - \vec{\rho}'|}\right) dl'\right] dl \end{aligned} \tag{34}$$

$$B_n = \sum_{j1=1}^{J}\int_{l_{j1}} g_{n-1}[\Omega_2^{-1}(\vec{\rho})]V_c(\vec{\rho})\, dl \tag{35}$$

for those $g_{n-1}[\Omega_2^{-1}(\vec{\rho})]$ defined on the conductor-to-dielectric interfaces, and

$$\begin{aligned} A_{nm} = \sum_{j1=1}^{J}\int_{l_{j1}} & g_{n-1}[\Omega_2^{-1}(\vec{\rho})] \\ & \cdot \left[\frac{\epsilon^+(\vec{\rho}) + \epsilon^-(\vec{\rho})}{2\epsilon_0[\epsilon^+(\vec{\rho}) - \epsilon^-(\vec{\rho})]} g_{m-1}(\vec{\rho})[\Omega_2^{-1}(\vec{\rho})] \right. \\ & + \frac{1}{2\pi\epsilon_0}\sum_{j2=1}^{J}\int\!\!\!\!\!\!-_{l_j} g_{m-1}[\Omega_2^{-1}(\vec{\rho}')] \\ & \left. \cdot \left(\frac{\vec{\rho} - \vec{\rho}'}{|\vec{\rho} - \vec{\rho}'|^2} - \frac{\vec{\rho} - \vec{\rho}''}{|\vec{\rho} - \vec{\rho}''|^2}\right) \cdot \hat{n}(\vec{\rho})\, dl'\right] dl \end{aligned} \tag{36}$$

$$B_n = 0 \tag{37}$$

for those $g_{n-1}[\Omega_2^{-1}(\vec{\rho})]$ defined on the dielectric-to-dielectric interfaces.

D. Evaluation of Integrals

In practice, integrals in (34)–(36) can be evaluated numerically in either the ζ domain or the ξ domain. We choose the ξ domain for our numerical computations as in the conventional

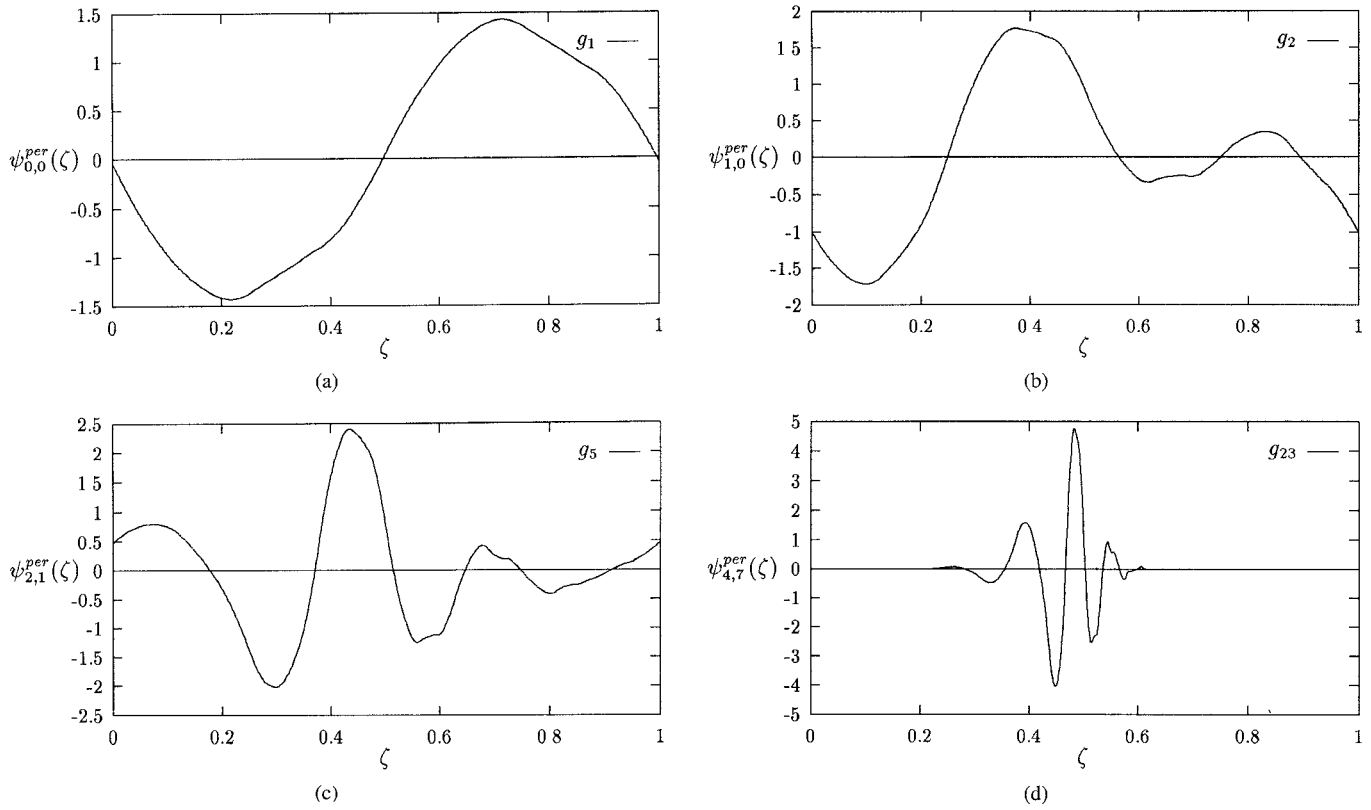

Fig. 3. The periodized wavelet constructed from Daubechies' orthogonal wavelet with $N = 5$ on the real line. (a) $g_1(x)$ $(\psi^{per}_{0,0}(x))$; (b) $g_2(x)$ $(\psi^{per}_{1,0}(x))$; (c) $g_5(x)$ $(\psi^{per}_{2,1}(x))$; and (d) $g_{23}(x)$ $(\psi^{per}_{4,7}(x))$.

boundary element analysis. Without loss of generality, let us consider the following integral:

$$T_{l_j}(\vec{\rho}_0) = \int_{l_j} g_{m-1}[\Omega_2^{-1}(\vec{\rho})]R(\vec{\rho}_0, \vec{\rho})\, dl. \tag{38}$$

Note that the integrals in (34)–(36) either are or consist of the above one-dimensional integral with a particular form of the kernel function $R(\vec{\rho}_0, \vec{\rho})$. Using the maps (30), (27), and (28), we have

$$T_{l_j}(\vec{\rho}_0) = \sum_{k=1}^{k=K_j} \int_0^1 g_{m-1}[\zeta_{k-1} + (\zeta_k - \zeta_{k-1}) \cdot \xi] \cdot R[\vec{\rho}_0, \Omega_1(\xi)]|D|\, d\xi \tag{39}$$

where $|D|$ is the Jacobian of the transformation between the global coordinates $\vec{\rho}$ and the local coordinate ξ of the kth standard element of contour l_j.

The Jacobian that defines the map of (27) can be obtained from the expression for the differential length

$$dl = \sqrt{(dx)^2 + (dy)^2} = \left[\sqrt{\left(\frac{dx}{d\xi}\right)^2 + \left(\frac{dy}{d\xi}\right)^2}\right] d\xi. \tag{40}$$

The Jacobian is then calculated from the following equation:

$$|D| = \sqrt{(D_x)^2 + (D_y)^2} \tag{41}$$

where

$$D_x = \frac{dx}{d\xi} = \sum_{i=1}^{M_e} \frac{dN_i(\xi)}{d\xi} x_i \tag{42}$$

$$D_y = \frac{dy}{d\xi} = \sum_{i=1}^{M_e} \frac{dN_i(\xi)}{d\xi} y_i \tag{43}$$

where x_i and y_i are, respectively, the x and y components of $\vec{\rho}_i$.

After computing the orthogonal wavelet on the real line by using the algorithms provided in the wavelet literature (e.g., [20], [21]), one can use definitions (10), (11), and (15) to obtain the periodic orthogonal wavelet $\{g_{m-1}(\zeta)\}$. Integration (39) is readily performed by standard numerical algorithms such as Gaussian quadratures [27].

V. Numerical Examples

Based on the technique proposed in the preceding sections, a program has been designed to compute the capacitance and inductance matrices of multiconductor transmission lines in multilayered dielectrics. Several numerical examples are presented in this section. In contrast to the use of wavelets on the real line to solve problems with finite intervals (where improper selection of the wavelets may result in nonphysical solutions), any type of wavelets on the real line can be used for the construction of the wavelets in $\boldsymbol{L}^2([0, 1])$ although there may be some discrepancies in their smoothness. However, since the derivatives of the unknown function $\sigma_T(\vec{\rho})$ are

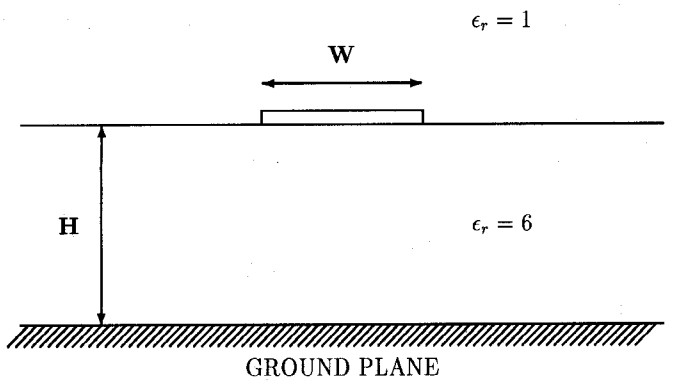

Fig. 4. Single infinitesimally thin microstrip line.

TABLE I
CHARACTERISTIC IMPEDANCES FOR THE THIN MICROSTRIP LINE

W/H	A	B	BEM	MOM	Hammerstad
0.4	90.5779	91.3783	90.7758	92.2785	90.3339
0.7	72.9504	73.2748	73.0898	73.9626	72.7516
1.0	62.0383	62.3342	62.1102	62.8109	61.8397
2.0	42.4233	42.5918	42.4118	42.9980	42.2600
4.0	26.5482	26.6498	26.5236	26.9709	26.4593
10.	12.7707	12.8134	12.7351	12.9961	12.7198

TABLE II
CAPACITANCE AND INDUCTANCE FOR THE CONFIGURATION OF FIG. 6

	This work	BEM	MOM	Analytical	Units
C	169.9379	169.9840	153.1754	170.1889	pF/m
L	353.0701	352.9743	391.7078	352.5494	nH/m

of order zero in the integral equations under consideration, a set of basis functions with C^0 continuity is sufficient to yield a convergent solution. In the following calculations, the Daubechies' wavelets (one type of orthogonal wavelets with compact support on the real line [20], [23]) are employed to construct the orthogonal wavelets in $L^2([0, 1])$. Fig. 3 depicts the periodized orthogonal wavelet constructed from the Daubechies' wavelet with $N = 5$.

Example 1—Thin microstrip line: An infinitesimally thin microstrip line, as illustrated in Fig. 4, was studied in this example. The characteristic impedances obtained by this technique were compared with those from the conventional boundary element method (BEM) [18], the method of moments (MOM) [15], and the more accurate formulas from [25] in Table I. The results of the conventional BEM were obtained by using sixteen subsections (33 bases) on the strip and thirty subsections (62 bases) at the dielectric interface, and those of the MOM were obtained by using twelve subsections on the strip and thirty subsections at the dielectric interface. Two sets of the results from this technique are presented in Columns A and B, with $M_1 = M_2 = 32$ and $M_1 = M_2 = 16$, respectively, where M_1 is the number of the wavelet bases used on the strip, while M_2 is the number at the dielectric interface.

Table I reveals an interesting insight to the wavelet expansions. Using the column labeled "Hammerstad" as a set of "ground truth" or standard references, the results from this technique with 64 bases (column A) give approximately the same accuracy as the conventional BEM, although the BEM results are obtained by using about 50% more (total 95) bases. The results from this technique with 32 bases (column B) exhibit better accuracy than the MOM even if the MOM uses approximately one third more (total 42) bases for its calculations. Finally, the comparison between the results of column A and column B shows that this technique with higher resolution approximation gives better accuracy.

Theoretically, it is not a surprise that the wavelet expansions converge faster, i.e., fewer coefficients are needed to represent a given function than other expansions, since this is a well known result from wavelet theory and has been extensively studied [21]–[23], [26]. One of the most attractive features of wavelets is that they give completely local information on the functions analyzed. It can be shown that, if the smoothness of a function is not everywhere the same (for instance, smooth functions with discontinuities), there is an optimal way to approximate the function using low resolution wavelets everywhere and adding high resolution wavelets near the singularities [22].

Since this technique is a wavelet-base method, as was expected, the matrix $[A]$ from this technique is sparse. Fig. 5 shows the matrices generated by this technique with 64 bases and the boundary element method with 95 bases, for the case of $W/H = 0.4$. It is quite apparent that the matrix $[A]$ from this technique is smaller and more sparse than that from the BEM, as illustrated in Fig. 5. The reason of having smaller matrix $[A]$ for this technique is because less bases are required for this technique than the BEM. It can be observed from Fig. 5 that, if a threshold of 10^{-3} is set, the matrix from this technique gives a quite sparse matrix since only a few of its entries are above the threshold 10^{-3}, while the matrix from the BEM turns out a full matrix. The advantage of having a sparse matrix over a full matrix is important, since sparse matrix solvers (e.g., see [27]) are much faster and need much smaller storage space than general matrix solvers. This advantage becomes more profound as a large matrix system is involved.

Interestingly, if a threshold of 10^{-2} is set, the sparsity can also be observed at the lower part (rows 34 to 95) of matrix $[A]$ from the BEM in Fig. 5(b). The lower part (rows 34 to 95) is generated by (18) (on the dielectric-to-dielectric interface). In fact, due to the prevailing contribution from its first term, the integral (18) is likely to yield sparse linear algebraic equations for subsectional basis methods (e.g., finite element method, boundary element method, moment method with subsection basis), which is usually a behavior of differential equations. Thus (18) does not take full advantage of the wavelet-base method as far as the sparsity issue is concerned, although there still may be some improvement to the sparsity in the lower part of matrix $[A]$ when this technique is compared with the BEM.

Example 2—Wire above ground plane problem: For curved surfaces, the BEM is more versatile and accurate than the MOM of [15], since the BEM matches the curved surfaces much better [18]. To demonstrate that this technique preserves the merit of the conventional BEM as well, the comparison of the results from this technique, the conventional BEM, the MOM and the analytical method for the wire-above-ground-

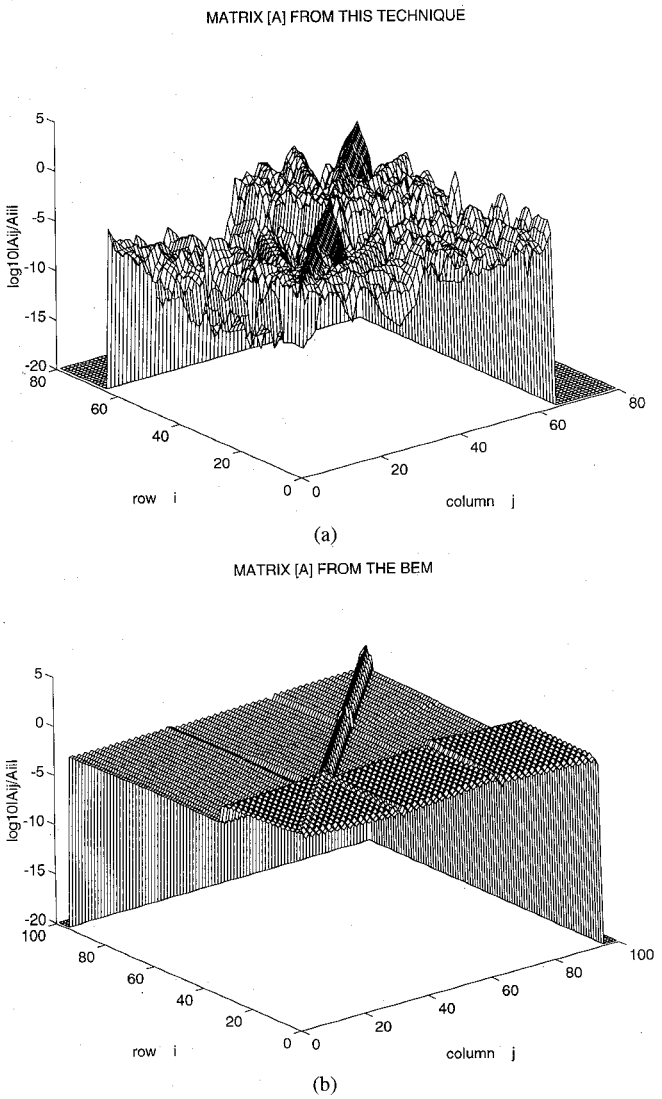

Fig. 5. 3-D logarithmic plots of the magnitudes of the entries in matrix $[A]$ for the case of $W/H = 0.4$ in example 1. (a) By this technique. (b) By the conventional boundary element method.

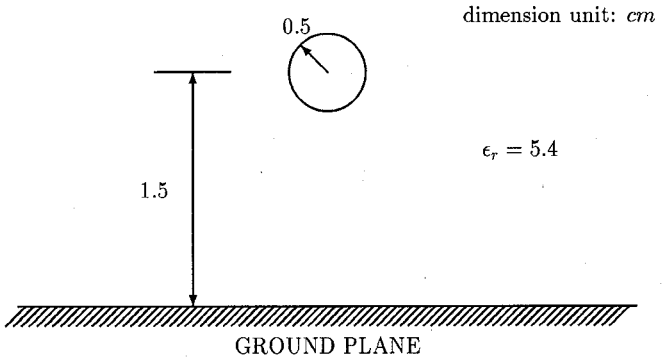

Fig. 6. Circular wire above ground plane.

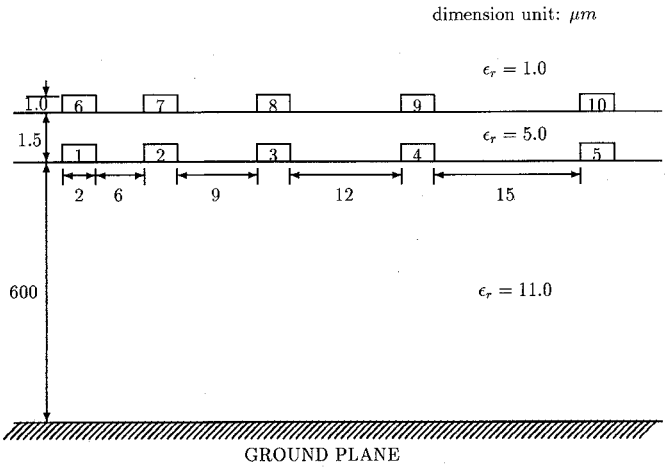

Fig. 7. Ten-conductor transmission line system above a thick dielectric substrate.

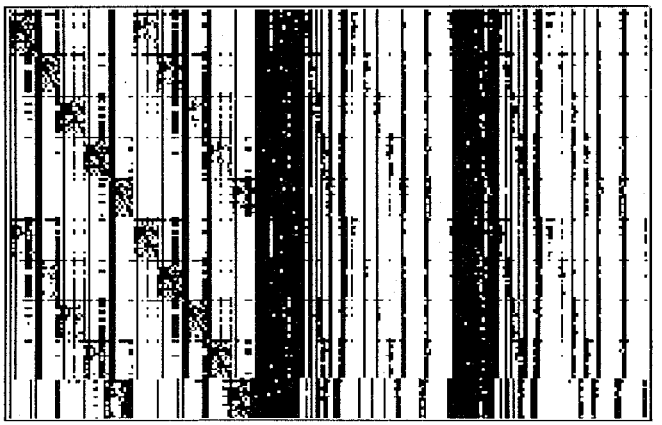

Fig. 8. Sparsity structure in the upper part of matrix $[A]$ in Example 3, which is generated by (17) from the technique described in this paper.

plane problem (see Fig. 6) is illustrated in Table II. The results of the conventional BEM, the MOM, and the analytical method are quoted from [18]. Both the BEM and MOM solutions were obtained by subdividing the circular cross section conductor into four subsections, as did the solution based upon this technique. Four wavelet bases are used along the contour of the conductor for the solution employing this technique, versus eight bases used for the conventional BEM.

Example 3—Multiconductor transmission line system with a thick substrate: This problem arises during the modeling of CMOS chips, where the transmission lines are far above the ground plane in comparison to the cross-sectional dimensions or the separations of the individual conductors. For such structures, the MOM approach frequently yields either singular matrices or nonphysical solutions [18]. In order to test the stability of this technique, we applied it to a ten conductor transmission line with a thick substrate, as depicted in Fig. 7. Table III lists the resulting capacitance and inductance matrices computed by this technique and the BEM with special edge treatment [18]. The BEM solutions were computed by using 160 subsections (360 bases) on the conductor surfaces and 190 subsections (392 bases) at the dielectric interfaces, and are quoted from [18]. The results from this technique were obtained by using 160 bases on the conductor surfaces and 256 bases at the dielectric interfaces. The self-capacitance of the ith conductor can be obtained by summing up all the elements at the ith row of the capacitance matrix $[C]$. Each of the self-capacitance values should be positive; otherwise, the results must be nonphysical solutions.

TABLE III
CAPACITANCE AND INDUCTANCE MATRICES FOR THE CONFIGURATION OF FIG. 7

A. This Technique:

Capacitance matrix $[C]$ (Unit: pF/m)

307.4 −41.10 −11.35 −6.330 −5.452 −219.6 −4.932 −1.389 −.8246 −.7600
−41.12 319.7 −27.96 −7.812 −5.043 −4.999 −217.5 −3.485 −.9775 −.6821
−11.35 −27.96 309.9 −24.24 −8.632 −1.377 −3.474 −218.4 −3.103 −1.154
−6.316 −7.794 −24.23 302.3 −24.70 −.8192 −.9580 −3.117 −218.9 −3.304
−5.440 −5.029 −8.624 −24.74 290.2 −.7487 −.6584 −1.136 −3.259 −221.5
−218.8 −5.019 −1.373 −.8105 −.7303 231.7 −2.063 −.3899 −.1799 −.1349
−4.967 −216.6 −3.492 −.9523 −.6406 −2.064 231.6 −1.176 −.2495 −.1332
−1.386 −3.526 −217.3 −3.150 −1.127 −.3896 −1.178 230.6 −.8550 −.2383
−.8200 −.9843 −3.162 −217.6 −3.306 −.1803 −.2511 −.8580 229.6 −.7478
−.7467 −.6755 −1.154 −3.343 −220.5 −.1358 −.1351 −.2399 −.7465 230.4

Inductance matrix $[L]$ (Unit: nH/m)

1407. 999.8 831.9 721.3 638.0 1306. 998.7 831.8 721.4 638.1
999.8 1405. 935.1 774.8 671.7 998.7 1304. 934.7 774.8 671.8
831.9 935.1 1407. 888.0 731.7 831.8 934.7 1307. 887.7 731.8
721.3 774.8 888.0 1409. 850.2 721.4 774.8 887.7 1309. 850.1
638.0 671.7 731.7 850.2 1411. 638.1 671.8 731.8 850.1 1310.
1306. 998.7 831.8 721.4 638.1 1407. 1000. 832.1 721.6 638.3
998.7 1304. 934.7 774.8 671.7 1000. 1405. 935.4 775.1 671.9
831.8 934.7 1307. 887.7 731.8 832.1 935.4 1408. 888.2 732.0
721.4 774.8 887.7 1309. 850.1 721.6 775.1 888.2 1410. 850.5
638.1 671.8 731.8 850.1 1310. 638.3 671.9 732.0 850.5 1411.

B. BEM Solution:

Capacitance matrix $[C]$ (Unit: pF/m)

308.5 −41.50 −11.42 −6.335 −5.417 −219.6 −5.019 −1.402 −.8288 −.7474
−41.51 321.2 −28.25 −7.853 −5.038 −5.081 −217.8 −3.577 −.9985 −.6799
−11.43 −28.25 312.0 −24.48 −8.665 −1.384 −3.539 −219.2 −3.214 −1.164
−6.339 −7.854 −24.47 304.9 −24.93 −.8126 −.9598 −3.198 −220.3 −3.382
−5.417 −5.036 −8.660 −24.92 291.8 −.7275 −.6423 −1.137 −3.360 −222.1
−220.3 −5.073 −1.380 −.8094 −.7240 233.4 −2.090 −.3937 −.1811 −.1332
−5.019 −218.7 −3.542 −.9590 −.6409 −2.091 233.9 −1.201 −.2544 −.1336
−1.403 −3.580 −220.2 −3.200 −1.137 −.3943 −1.201 233.7 −.8819 −.2420
−.8282 −.9984 −3.216 −221.3 −3.363 −.1814 −.2545 −.8820 233.5 −.7688
−.7448 −.6777 −1.162 −3.377 −222.9 −.1333 −.1335 −.2417 −.7683 233.0

Inductance matrix $[L]$ (Unit: nH/m)

1398. 993.1 826.2 716.5 633.7 1297. 992.1 826.2 716.6 633.8
993.0 1396. 928.8 769.5 667.1 992.1 1295. 928.4 769.6 667.2
826.2 928.9 1398. 881.9 726.7 826.2 928.4 1298. 881.8 726.8
716.5 769.6 882.0 1400. 844.5 716.6 769.7 881.8 1300. 844.4
633.7 667.1 726.8 844.5 1402. 633.9 667.3 726.9 844.4 1301.
1297. 992.0 826.2 716.5 633.8 1398. 993.4 826.6 716.8 634.0
992.0 1295. 928.4 769.6 667.2 993.4 1396. 929.1 769.9 667.4
826.2 928.4 1298. 881.7 726.8 826.6 929.2 1399. 882.3 727.1
716.6 769.6 881.7 1299. 844.3 716.8 769.9 882.3 1401. 844.8
633.8 667.2 726.8 844.4 1301. 634.0 667.5 727.1 844.8 1402.

The sizes of matrix $[A]$ are, respectively, 752 × 752 and 416 × 416 for the BEM and this technique. For such a relatively large matrix $[A]$, the sparsity is more significant. As mentioned in Example 1, (18) is likely to produce sparse linear algebraic equations for both the wavelet-base approach and the BEM. Hence, we will only examine the sparsity for the upper part of matrix $[A]$, which comes from (17). Fig. 8 shows the upper part of matrix $[A]$ obtained by using this technique under a threshold of 10^{-3}, which is a 160 × 416 sparse matrix, in sharp contrast to a 360 × 752 full dense matrix generated by the BEM under the same threshold.

VI. CONCLUSION

In this paper, a hybrid wavelet expansion and boundary element technique was introduced to investigate multiconductor transmission line systems in multilayered dielectric media. The set of integral equations under consideration is solved by Galerkin's method, with the unknown total charge expanded in terms of orthogonal wavelets in $L^2([0, 1])$. To treat the curved surfaces, the geometric representation in the boundary element method has been incorporated into this analysis. It has been demonstrated that this technique exhibits the advantages of

both the wavelet expansion method and the boundary element method. That is, this technique possesses the properties of rapid convergence, a sparse matrix system and the ability to model curved surfaces accurately.

ACKNOWLEDGMENT

The authors wish to thank Dr. J. Murphy, ARPA/ESTO, Dr. R. Pohanka and Dr. L. Kabacoff, ONR, and Dr. P. Young, Boeing High Technology Center, for support and helpful discussions.

REFERENCES

[1] S. G. Mallat, "A theory for multiresolution signal decomposition: The wavelet representation," *IEEE Trans. Pattern Anal. Machine Intell.*, vol. 11, pp. 674–693, July 1990.
[2] M. Vetterli, "Wavelets and filter banks for discrete-time signal processing," in *Wavelets and its Applications*, M. B. Ruskai *et al.*, Eds. Boston, MA: Jones and Bartleth, 1992, pp. 17–52.
[3] G. Wang, J. Zhang, and G. Pan, "Solution of inverse problems in image processing by wavelet expansion," *IEEE Trans. Image Processing*, to be published.
[4] D. S. Wang, G. Welland, and S. Zhao, "Modeling of three dimensional scattering using large curvilinear triangular patches and wavelet expansion functions," in *1992 URSI Radio Sci. Meet. Dig.*, Chicago, IL, July 1992, p. 338.
[5] R. L. Wagner, G. P. Otto, and W. C. Chew, "Fast waveguide mode computation using wavelet-like basis functions," *IEEE Microwave and Guided Wave Lett.*, vol. 3, pp. 208–210, July 1993.
[6] B. Z. Steinberg and Y. Leviatan, "On the use of wavelet expansions in the method of moments," *IEEE Trans. Antennas Propagat.*, vol. 41, pp. 610–619, May 1993.
[7] G. Wang and G. Pan, "Full wave analysis of microstrip floating line structures by wavelet expansion method," *IEEE Trans. Microwave Theory Tech.*, vol. MTT-43, pp. 131–142, Jan. 1995.
[8] G. Beylkin, R. R. Coifman, and V. Rokhlin, "Fast wavelet transforms and numerical algorithms I," Yale University Technical Report, YALEU/DCS/RR-696, Aug. 1989, *Comm. on Pure Appl. Math.*, vol. XLIV, pp. 141–183, 1991.
[9] M. J. Tsuk and J. A. Kong, "A hybrid method for the calculation of the resistance and inductance of transmission lines with arbitrary cross sections," *IEEE Trans. Microwave Theory Tech.*, vol. 39, pp. 1338–1347, Aug. 1991.
[10] M. A. Mehalic and R. Mittra, "Investigation of tapered multiple microstrip lines for VLSI circuits," *IEEE Trans. Microwave Theory Tech.*, vol. 38, pp. 1559–1567, Nov. 1990.
[11] R. E. Collin, *Field Theory of Guided Waves*, 2nd ed. New York: IEEE Press, 1991, pp. 305–332.
[12] R. W. Jackson and D. M. Pozar, "Full-wave analysis of microstrip open-end and gap discontinuities," *IEEE Trans. Microwave Theory Tech.*, vol. MTT-33, pp. 1036–1042, Oct. 1985.
[13] G. Pan, J. Tan, and J. Murphy, "Full-wave analysis of microstrip floating line discontinuities," *IEEE Trans. Electromagnet. Compat.*, vol. 36, no. 1, pp. 49–59, Feb. 1994.
[14] G. Pan, K. Olson, and B. Gilbert, "Improved algorithmic method for the prediction of wavefront propagation behavior in multiconductor transmission lines in multilayered dielectric media," *IEEE Trans. Computer-Aided Design*, vol. 8, pp. 608–621, June 1989.
[15] C. Wei, R. F. Harrington, J. R. Mautz, and T. K. Sarkar, "Multiconductor transmission lines in multilayered dielectric media," *IEEE Trans. Microwave Theory Tech.*, vol. MTT-32, pp. 439–449, Apr. 1984.
[16] W. Delbare and D. D. Zutter, "Space-domain Green's function approach to the capacitance calculation of multiconductor lines in multilayered dielectrics with improved surface charge modeling," *IEEE Trans. Microwave Theory Tech.*, vol. 37, pp. 1562–1568, Oct. 1989.
[17] G. Pan, G. Wunsch, and B. Gilbert, "Frequency-domain analysis of coupled nonuniform transmission lines using Chebyshev pseudo-spatial techniques," *IEEE Trans. Microwave Theory Tech.*, vol. 40, pp. 2025–2033, Nov. 1992.
[18] G. Pan, G. Wang, and B. Gilbert, "Edge effect enforced boundary element analysis of multilayered transmission lines," *IEEE Trans. Circuits Syst I: Fundamental theory and applications*, vol. 39, pp. 955–963, Nov. 1992.
[19] B. K. Gilbert and L. Salmon, "Interconnection design and process characteristics for digital multichip modules operating at high system clock rates," in *Thin Film Multichip Modules*, G. Messner, I. Turlik, J. Balde, and P. Garrou, Eds. Reston, VA: ISHM, 1992, ch. 5.
[20] I. Daubechies, *Ten Lectures on Wavelet*. SIAM, 1992.
[21] C. K. Chui, *An Introduction to Wavelets*. New York: Academic, 1991.
[22] ——, Ed., *Wavelets—A Tutorial in Theory and Applications*. New York: Academic, 1992.
[23] I. Daubechies, "Orthonormal bases of compactly supported wavelets," *Commun. Pure Appl. Math.*, vol. 41, pp. 909–996, Nov. 1988.
[24] C. A. Brebbia, J. C. F. Telles, and L. C. Wrobel, *Boundary Element Techniques*. Berlin: Springer-Verlag, 1984.
[25] E. Hammerstad and O. Jensen, "Accurate models for microstrip computer-aided design," in *IEEE MTT-S Int. Microwave Symp. Dig.*, Washington, DC, 1980, pp. 407–409.
[26] G. G. Walter, "Pointwise convergence of wavelet expansions," preprint, 1992.
[27] C. C. Paige and M. A. Saunders, "LSQR: An algorithm for sparse linear equations and sparse least squares," in *ACM Trans. Mathematical Software*, vol. 8, no. 1, pp. 43–71, Mar. 1982.

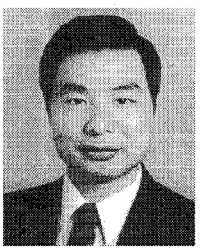

Gaofeng Wang was born in Hubei, China, on December 24, 1965. He received the B.S. degree in physics from the Hubei University and the M.S. degree in space and radio physics from the Wuhan University, Wuhan, China, in 1983 and 1988, respectively, and the Ph.D degree in electrical engineering with minors in mathematics and computer science from the University of Wisconsin at Milwaukee (UWM) in 1993.

From 1988 to 1990 he was with the Department of Space Physics, Wuhan University, where was involved in research and teaching of radiowave propagation in ionosphere and numerical methods for electromagnetic waves and fields. From 1990 to 1993 he was a research assistant in the Department of Electrical Engineering at UWM. Currently, he is a Scientist in the Tanner Research, Inc., Pasadena, CA. His research interests include numerical techniques for electromagnetic computations, signal integrity analysis of electronic systems and wavelet applications in numerical analysis and image processing.

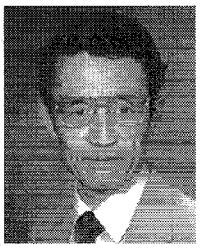

Guangwen Pan (S'81–S'83–M'84–SM'94) received the B.E. degree in mechanical engineering from Peking Institute of Petroleum Technology in 1967. He attended the Graduate School, University of Science and Technology of China from 1978 to 1980, majoring in electrical engineering. He received the M.S. degree in 1982, and the Ph.D. degree in 1984, both in electrical engineering, from the University of Kansas, Lawrence, KS.

He worked at the Institute of Development and Research in the Northwest of China in machine design as an associate engineer, and then as an electrical engineer responsible for design of pulse-width modulation electronics and digital remote fire control systems used in petroleum seismic exploration. He came to the United States in August 1980 as a research assistant in the Remote Sensing Laboratory, University of Kansas. From September 1984 to May 1985, he was a post-doctoral fellow at the University of Texas, engaged in a project on computer-aided design of airborne antenna/radome systems. He joined Mayo Foundation in 1985, engaged in theoretical modeling of the electromagnetic behavior of high-speed integrated circuits, electronic circuit boards, and high density substrates, placement and routing. From 1986 to 1988 he was an associate professor in the Department of Electrical Engineering, South Dakota State University. In 1988, he joined the Department of Electrical Engineering and Computer Science at the University of Wisconsin–Milwaukee as an associate professor. He has been the Director of the Signal Propagation Research Laboratory since 1990 and became a professor in 1993. His research interests continue to be in the mathematical modeling of the electromagnetic environment of high clock rate signal processors. He is cited in *Who's Who in America* and *Who's Who in the World*.

Dr. Pan is a memeber of the Editorial Board of IEEE TRANSACTIONS ON MICROWAVE THEORY AND TECHNIQUES and a member of Eta Kappa Nu.

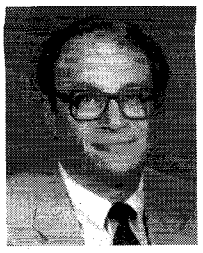

Barry K. Gilbert (S'62–M'70–SM'87) received the B.S. degree in electrical engineering from Purdue University, Lafayette, IN, in 1965, and the Ph.D. degree in physiology and biophysics with minors in applied mathematics and electrical engineering, from the University of Minnesota, Minneapolis, MN, in 1972.

He is presently a Staff Scientist and Professor in the Department of Physiology and Biophysics, Mayo Foundation, Rochester, MN. His research interests include the design of special-purpose digital processors for high-speed signal processing and the development of advanced integrated circuit and electronic packaging technologies to support real-time signal processing of extremely wideband data. He has worked on a variety of projects, including the development in the mid 1970's of a very wideband special-purpose digital data handling and array processing computer fabricated entirely with subnanosecond emitter coupled logic and a special-purpose multiple instruction, multiple data (MIMD) processor capable of operating with up to 30 coprocessors under parallel microcode control in the late 1970's. More than 25 digital Gallium Arsenide (GaAs) chips have been designed in his laboratory during the past decade, most recently a GaAs Heterojunction Bipolar Transistor (HBT) chip capable of operating at 6 GHz clock rates. A half dozen industrial collaborations have been conducted to insert GaAs chips into existing signal processors. Recently, his group has designed a family of multichip modules (MCM's), which have demonstrated their ability to support the operation of multiple interconnected GaAs chips at system clock rates of up to 2.5 GHz. His research group has been developing electromagnetic modeling tools for printed circuit boards, MCM's, and integrated circuits since 1980; these tools are presently being distributed to both universities and large corporations. He is currently responsible for the development of CAD tools at the system and GaAs integrated circuit levels, as well as high-density electronic packaging technologies based on deposited and laminated metal-organic MCM's, which will allow the fabrication of signal processing modules operating at multi-GHz clock rates.